Journal of Computational Physics 291 (2015) 317–333

Contents lists available at ScienceDirect

Journal of Computational Physics

www.elsevier.com/locate/jcp

Comparison of efficient techniques for the simulation of dielectric objects in electrolytes

Zecheng Gan [a,1], Huanxin Wu [b,1], Kipton Barros [c], Zhenli Xu [a], Erik Luijten [b,d,e,*]

[a] Department of Mathematics, Institute of Natural Sciences, and MoE Key Lab for Scientific and Engineering Computing, Shanghai Jiao Tong University, Shanghai 200240, People's Republic of China
[b] Department of Physics and Astronomy, Northwestern University, Evanston, IL 60208, USA
[c] Theoretical Division and CNLS, Los Alamos National Laboratory, Los Alamos, NM 87545, USA
[d] Department of Engineering Sciences and Applied Mathematics, Northwestern University, Evanston, IL 60208, USA
[e] Department of Materials Science and Engineering, Northwestern University, Evanston, IL 60208, USA

ARTICLE INFO

Article history:
Received 18 September 2014
Received in revised form 7 March 2015
Accepted 11 March 2015
Available online 17 March 2015

Keywords:
Boundary-element method
Image-charge method
Electrostatic polarization
Molecular dynamics simulations
Monte Carlo simulations

ABSTRACT

We review two recently developed efficient approaches for the numerical evaluation of the electrostatic polarization potential in particle-based simulations. The first is an image-charge method that can be applied to systems of spherical dielectric objects and provides a closed-form solution of Poisson's equation through multiple image-charge reflections and numerical evaluation of the resulting line integrals. The second is a boundary-element method that computes the discretized surface bound charge through a combination of the generalized minimal residual method (GMRES) and a fast Ewald solver. We compare the accuracy and efficiency of both approaches as a function of the pertinent numerical parameters. We demonstrate use of the image-charge method in a Monte Carlo simulation using the Barnes–Hut octree algorithm and the boundary-element method in a molecular dynamics simulation using the Particle–Particle Particle–Mesh (PPPM) Ewald method, and present numerical results for the ensemble-averaged induced force between two spherical colloids immersed in an electrolyte.

1. Introduction

Electrostatic interactions are of fundamental importance for understanding the structure–function relationships of many physical and biological systems, including colloidal suspensions, membranes, biopolymers, and energy devices [1–3]. All-atom computer simulations of such systems are generally prohibitively expensive, due to the required repeated evaluation of the forces or internal energies of molecular configurations. Thus, continuum approximations and coarse-grained models are often adopted. For example, the solvent is usually treated as an implicit continuum described by a (static) dielectric permittivity. The ion distributions in this solvent can be described by mean-field approximations such as the Poisson–Boltzmann theory and its modifications [4–7]. These continuum models have been widely used, but are only accurate in limited parameter regimes, as polarization and many-body effects are often ignored.

* Corresponding author at: Department of Materials Science and Engineering, Northwestern University, Evanston, IL 60208, USA.
E-mail addresses: xuzl@sjtu.edu.cn (Z. Xu), luijten@northwestern.edu (E. Luijten).
[1] Z.G. and H.W. contributed equally to this work.

http://dx.doi.org/10.1016/j.jcp.2015.03.019
0021-9991/

Alternatively, water can be treated in the continuum approximation, whereas the ions are treated as discrete particles, incorporating ionic correlations and ion-size effects. This coarse-graining strategy, the so-called primitive model for electrolytes, is commonly employed in particle-based molecular dynamics (MD) or Monte Carlo (MC) simulations (see, e.g., [8,9]). Although this is a powerful approach, a formidable computational challenge that remains is the rapid calculation of electrostatic polarization due to the dielectric mismatch at material interfaces, such as the dielectric contrast between the implicit solvent and the solutes. Polarization is relevant in a wide range of systems, including colloidal suspensions [10–12], cloud droplets [13,14], and protein folding and stabilization [15]. Determination of the polarization field through analytical solution of Poisson's equation is very difficult. Closed-form representations, in the form of harmonic series, of the Green's function are known only for specific geometries such as planar, spherical, and cylindrical interfaces [16–19,11,20,21]. Moreover, even if the closed-form Green's function is employed, the computation of the harmonic series during simulations can still be too expensive if large systems are investigated.

For these reasons, methods for the determination of electrostatic polarization at dielectric interfaces have attracted significant renewed attention [11,22–25,12]. In certain cases, it is possible to avoid the evaluation of harmonic series via an image-charge representation of the closed-form Green's functions [26–30]. Recently, this *image-charge method* (ICM) has been extended to the treatment of multiple spheres via recursive reflections [31]. This approach not only provides a fast approximation to the Green's function, but also can be easily accelerated by well-known algorithms, because the approximation is a sum of Coulomb potentials. Alternatively, various approaches to direct numerical solution of the Poisson equation using the *boundary-element method* (BEM) have been proposed [32–39,25]. The BEM offers the advantage that arbitrary geometries can be handled with relative ease. Moreover, the BEM facilitates the treatment of periodic geometries commonly employed in electrostatics problems.

Here, two recently developed adaptations of both approaches are investigated in detail. The BEM for general mobile dielectric objects was proposed and implemented in [25,12] for MD simulations. The ICM for multiple spheres was presented in [31]; here we present its first implementation within a MC simulation. For the BEM, surface bound charge is obtained from the solution of a dense linear system via the generalized minimum residual (GMRES) method [40], using a formulation that is particularly well conditioned [41,25]. Moreover, the matrix–vector product required in each GMRES iteration is accelerated by a fast Ewald solver, in our implementation the particle–particle particle–mesh (PPPM) method [42,43] (but note that the BEM is independent of the choice of the solver). This combination of techniques yields a near-linear scaling calculation in the number of discrete boundary elements. For the ICM, the single-sphere image-charge formula is applied recursively using reflections between spheres. The singular or nearly singular quadrature problem for the image line charge integral has been well approximated. The image-charge number is chosen to achieve a specified accuracy at minimal cost. Thus, a set of image charges is constructed that represents the polarization potential. The Barnes–Hut octree algorithm [44–46] is used to efficiently calculate the interaction of a source charge with other charges, in a manner tailored for the single-particle displacements employed in MC simulations [47].

The relevance of polarization problems in wide areas of science makes it pressing to perform a quantitative comparison of the BEM and ICM methods in terms of accuracy, efficiency, and performance. To illustrate these algorithm properties, we present results for a representative problem, namely the ensemble-averaged mean force between a pair of colloidal particles immersed in an electrolyte. The mean force is typically employed to investigate the effective interactions between colloids (although typically without taking into account dielectric effects), and has attracted significant interest in recent years [48–54], due to its fundamental importance in colloidal science. We demonstrate how the simulations can decompose the total mean force into contributions arising from ion–polarization interactions, interactions between bound charges, and entropic effects.

This paper is organized as follows. We first describe the formulations of the BEM and ICM in Sections 2 and 3, respectively (with an error analysis of the ICM in Appendix A). Then, their computational complexity is compared in Section 4, followed by tests of the accuracy and parameter choices of both algorithms in Section 5. In Section 6, we present a practical illustration in the form of MD and MC simulation results for the induced mean force between dielectric colloidal spheres. We conclude with a summary in Section 7.

2. Boundary-element method

Starting from the electrostatic field $\mathbf{E}$, we provide a brief derivation of the BEM presented in [25]. At an arbitrary location in the domain $V \in \mathbb{R}^3$, $\mathbf{E}$ satisfies the differential form of Gauss's law [55],

$$\nabla \cdot \mathbf{E}(\mathbf{r}) = \frac{\rho(\mathbf{r})}{\epsilon_0}\,, \tag{1}$$

and—if no time-dependent magnetic field is present—Faraday's law,

$$\nabla \times \mathbf{E}(\mathbf{r}) = \mathbf{0}\,, \tag{2}$$

where $\rho(\mathbf{r})$ is the total charge density and ϵ_0 the vacuum permittivity. From the Helmholtz decomposition,

$$\mathbf{E}(\mathbf{r}) = -\nabla\Phi(\mathbf{r})\,, \tag{3}$$

we arrive at Poisson's equation for the electrostatic potential $\Phi(\mathbf{r})$,

$$-\nabla^2\Phi(\mathbf{r}) = \frac{\rho(\mathbf{r})}{\epsilon_0} . \tag{4}$$

For convenience, we define the linear operator $\mathscr{G} = -\nabla^{-2}$, so that the solution of (4) can be represented as

$$\Phi(\mathbf{r}) = \frac{\mathscr{G}\rho(\mathbf{r})}{\epsilon_0} = \int_V G_0(\mathbf{r},\mathbf{r}')\rho(\mathbf{r}')d\mathbf{r}' , \tag{5}$$

where G_0 is the Green's function for (4), satisfying

$$-\epsilon_0\nabla^2 G_0(\mathbf{r},\mathbf{r}') = \delta(\mathbf{r}-\mathbf{r}') . \tag{6}$$

For free-space boundary conditions, $G_0 = 1/(4\pi\epsilon_0|\mathbf{r}-\mathbf{r}'|)$ is simply the Coulomb potential due to a unit source charge, whereas for periodic boundary conditions G_0 can be treated via the Ewald summation. Combining (3) and (5) we can represent the electric field as

$$\mathbf{E}(\mathbf{r}) = -\nabla\frac{\mathscr{G}\rho(\mathbf{r})}{\epsilon_0} . \tag{7}$$

We restrict ourselves to systems comprised of objects with linear and isotropic dielectric response, i.e., characterized by a spatially varying dielectric constant $\epsilon(\mathbf{r})$ or, equivalently, a local electric susceptibility $\chi(\mathbf{r}) = \epsilon(\mathbf{r})/\epsilon_0 - 1$. The local polarization field $\mathbf{P}$ induced by the electric field $\mathbf{E}$ is then given by the constitutive relation

$$\mathbf{P}(\mathbf{r}) = \epsilon_0\chi(\mathbf{r})\mathbf{E}(\mathbf{r}) . \tag{8}$$

As a result, the polarization charge associated with the polarization field reads

$$\rho_{\mathrm{pol}}(\mathbf{r}) = -\nabla\cdot\mathbf{P}(\mathbf{r}) = -\nabla\cdot[\epsilon_0\chi(\mathbf{r})\mathbf{E}(\mathbf{r})] . \tag{9}$$

Note that the total charge density ρ at location $\mathbf{r}$ consists of both free charge density and polarization charge density (also referred to as bound charge density),

$$\rho(\mathbf{r}) = \rho_{\mathrm{f}}(\mathbf{r}) + \rho_{\mathrm{pol}}(\mathbf{r}) . \tag{10}$$

In simulations of dielectric objects, $\rho_{\mathrm{f}}(\mathbf{r})$ is specified by the particle configuration, whereas the efficient calculation of $\rho_{\mathrm{pol}}(\mathbf{r})$ is our primary objective. In the following, we discuss how to construct a linear operator equation for the bound charge density.

Substitution of (3) into (9) yields

$$\begin{aligned}\rho_{\mathrm{pol}}(\mathbf{r}) &= \epsilon_0\nabla\cdot[\chi(\mathbf{r})\nabla\Phi(\mathbf{r})] \\ &= \epsilon_0\chi(\mathbf{r})\nabla^2\Phi(\mathbf{r}) + \epsilon_0\nabla\chi(\mathbf{r})\cdot\nabla\Phi(\mathbf{r}) .\end{aligned} \tag{11}$$

This implies that polarization charge may arise in two ways, namely nonzero divergence of the electric field, which corresponds to locations of free charge, and spatial variation of the electric susceptibility. The first term on the right-hand side of (11) can be reduced to $-\chi(\mathbf{r})\rho(\mathbf{r})$ with (4) and the second term can be rewritten as $-\nabla\epsilon(\mathbf{r})\cdot\mathbf{E}(\mathbf{r})$. Applying (10), we obtain

$$\frac{\epsilon(\mathbf{r})}{\epsilon_0}\left[\rho_{\mathrm{f}}(\mathbf{r}) + \rho_{\mathrm{pol}}(\mathbf{r})\right] + \nabla\epsilon(\mathbf{r})\cdot\mathbf{E}(\mathbf{r}) = \rho_{\mathrm{f}}(\mathbf{r}) , \tag{12}$$

which can be simplified via (1) to

$$\nabla\cdot\epsilon(\mathbf{r})\mathbf{E}(\mathbf{r}) = \rho_{\mathrm{f}}(\mathbf{r}) . \tag{13}$$

Here we have two choices for substituting the electric field $\mathbf{E}$. One choice is to substitute (3), resulting in an alternative form of Poisson's equation,

$$-\nabla\cdot\epsilon(\mathbf{r})\nabla\Phi(\mathbf{r}) = \rho_{\mathrm{f}}(\mathbf{r}) . \tag{14}$$

This formulation differs from (4) in two ways: The source term of this equation is simply the *free* charge density ρ_{f}, thus there is no need to solve for ρ_{pol}. In exchange, the position-dependent dielectric constant leads to a Green's function $\widetilde{G}$ that is no longer in simple Coulomb form like G_0. Instead, it satisfies

$$-\nabla\cdot\epsilon(\mathbf{r})\nabla\widetilde{G}(\mathbf{r},\mathbf{r}') = \delta(\mathbf{r}-\mathbf{r}') . \tag{15}$$

Thus, the solution for (14) can be represented as

$$\Phi(\mathbf{r}) = \int_V \widetilde{G}(\mathbf{r},\mathbf{r}')\rho_{\mathrm{f}}(\mathbf{r}')d\mathbf{r}' . \tag{16}$$

Here $\widetilde{G}$ in the exterior region (i.e., the region outside the dielectric objects, with relative permittivity ϵ_m) is a sum of two parts,

$$\widetilde{G}(\mathbf{r},\mathbf{r}') = \widetilde{G}_{\text{Coul}}(\mathbf{r},\mathbf{r}') + \widetilde{G}_{\text{pol}}(\mathbf{r},\mathbf{r}') \,, \tag{17}$$

where $\widetilde{G}_{\text{Coul}}(\mathbf{r},\mathbf{r}') = G_0(\mathbf{r},\mathbf{r}')/\epsilon_m$ is the Coulomb potential of a unit charge in a dielectric medium with permittivity ϵ_m and the polarization potential $\widetilde{G}_{\text{pol}}(\mathbf{r},\mathbf{r}')$ satisfies the Laplace equation,

$$\nabla^2 \widetilde{G}_{\text{pol}}(\mathbf{r},\mathbf{r}') = 0 \,. \tag{18}$$

Obviously, the difficulty in solving (14) lies in obtaining $\widetilde{G}_{\text{pol}}$, see Section 3.

On the other hand, the BEM employs a different approach to (13). We substitute (7) and define the operator

$$\mathscr{A} = -\nabla \cdot \frac{\epsilon(\mathbf{r})}{\epsilon_0} \nabla \mathscr{G} \tag{19}$$

to arrive at a linear equation linking the polarization charge density and the free charge density,

$$\mathscr{A}\rho_{\text{pol}} = b \,, \tag{20}$$

with

$$b = (1 - \mathscr{A})\rho_{\text{f}} \,, \tag{21}$$

where we have separated the bound charge from the free charge. Eq. (20) is applicable to general electrostatic problems in any isotropic and linear dielectric continuum, i.e., $\epsilon(\mathbf{r})$ can be any spatially varying function. However, its numerical solution requires discretization of the entire domain. The computational cost can be greatly reduced by exploiting the observation that for many physical systems the dielectric constant varies rapidly only at the interfaces between media. This justifies the approximation to confine ourselves to systems with sharp dielectric interfaces, where $\nabla\epsilon(\mathbf{r})$ is nonzero only at the interfaces.

Consider a model system consisting of $\mathscr{P}$ uniform dielectric objects $\mathscr{S}_i$ ($1 \le i \le \mathscr{P}$), embedded in a dielectric continuum. We assume that all objects are neither touching nor intersecting each other, i.e., $\mathscr{S}_i \bigcap \mathscr{S}_j = \varnothing$. The domain V can then be divided into an interior region $\Omega = \bigcup_{i=1}^{\mathscr{P}} \mathscr{S}_i$ and an exterior region $V \backslash \Omega$. Any free charge *within* Ω is replaced with free charge density σ_{f} at the object surfaces that produces the equivalent electric field in the exterior region (cf. [25, Sec. IV.I]). In addition, there is a bulk free charge density $\rho_{\text{f}}(\mathbf{r})$ in the exterior region. The dielectric constant $\epsilon(\mathbf{r})$ is set to be piecewise constant, with discontinuities only at the object interfaces,

$$\epsilon(\mathbf{r}) = \begin{cases} \epsilon_0\epsilon_i & \mathbf{r} \in \mathscr{S}_i, \\ \epsilon_0\epsilon_{\text{m}} & \mathbf{r} \in (V \backslash \Omega) \end{cases} \,, \tag{22}$$

where ϵ_i and ϵ_m are the relative permittivities of object i and the embedding medium, respectively. The polarization charge density $\rho_{\text{pol}}(\mathbf{r})$ due to variation of the dielectric constant is then only present on the object surfaces and reduces to the surface bound charge density $\sigma_{\text{pol}}(\mathbf{r})$.

To obtain a linear operator equation for $\sigma_{\text{pol}}(\mathbf{r})$ analogous to (20), we first recall the standard boundary condition for the electric displacement field at any point $\mathbf{r}$ on the object surfaces, as implied by (13),

$$\epsilon_0 \left[\epsilon_{\text{m}} \mathbf{E}_{\text{out}}(\mathbf{r}) - \epsilon_i \mathbf{E}_{\text{in}}(\mathbf{r})\right] \cdot \hat{\mathbf{n}} = \sigma_{\text{f}}(\mathbf{r}) \,, \tag{23}$$

where $\mathbf{E}_{\text{in}}(\mathbf{r})$ and $\mathbf{E}_{\text{out}}(\mathbf{r})$ are the electric field inside and outside the surface at point $\mathbf{r}$, respectively, and $\hat{\mathbf{n}}$ is the outward unit normal to the surface at $\mathbf{r}$. Likewise, (1) implies

$$\epsilon_0 \left[\mathbf{E}_{\text{out}}(\mathbf{r}) - \mathbf{E}_{\text{in}}(\mathbf{r})\right] \cdot \hat{\mathbf{n}} = \sigma_{\text{f}}(\mathbf{r}) + \sigma_{\text{pol}}(\mathbf{r}) \,. \tag{24}$$

Combining (23) and (24) and defining the electric field at the surface as $\mathbf{E}(\mathbf{r}) = [\mathbf{E}_{\text{in}}(\mathbf{r}) + \mathbf{E}_{\text{out}}(\mathbf{r})]/2$, we obtain

$$\bar{\epsilon}_i \left[\sigma_{\text{f}}(\mathbf{r}) + \sigma_{\text{pol}}(\mathbf{r})\right] + \epsilon_0 \Delta\epsilon_i \mathbf{E}(\mathbf{r}) \cdot \hat{\mathbf{n}} = \sigma_{\text{f}}(\mathbf{r}) \,, \tag{25}$$

where $\bar{\epsilon}_i = (\epsilon_i + \epsilon_m)/2$ and $\Delta\epsilon_i = \epsilon_m - \epsilon_i$. This has the same form as (12), except that it avoids the factor $\nabla\epsilon(\mathbf{r})$ which is ill-defined at the interface. Observe how free charge not located on the object surfaces enter this equation through the electric field $\mathbf{E}$. Finally, (25) is expressed in a linear form equivalent to (20),

$$\mathscr{A}_{\text{s}}\sigma_{\text{pol}} = b_{\text{s}} \,, \tag{26}$$

where

$$\mathscr{A}_{\text{s}}\sigma_{\text{pol}} \equiv \bar{\epsilon}_i \sigma_{\text{pol}} + \epsilon_0 \Delta\epsilon_i \mathbf{E}_{\text{pol}} \cdot \hat{\mathbf{n}} \,, \tag{27}$$

with

$$\mathbf{E}_{\text{pol}}(\mathbf{r}) = \sum_{i=1}^{\mathscr{P}} \int_{\partial\mathscr{S}_i} \frac{\sigma_{\text{pol}}(\mathbf{s}')(\mathbf{r} - \mathbf{s}')}{4\pi\epsilon_0 |\mathbf{r} - \mathbf{s}'|^3} d\mathbf{s}' \tag{28}$$

the polarization field from all surface polarization charge at $\mathbf{s}' \neq \mathbf{r}$ and

$$b_s = (1-\bar{\epsilon}_i)\sigma_f - \epsilon_0 \Delta\epsilon_i \mathbf{E}_f \cdot \hat{\mathbf{n}}\,, \tag{29}$$

with

$$\mathbf{E}_f(\mathbf{r}) = \sum_{i=1}^{\mathscr{P}} \int_{\partial\mathscr{S}_i} \frac{\sigma_f(\mathbf{s}')(\mathbf{r}-\mathbf{s}')}{4\pi\epsilon_0|\mathbf{r}-\mathbf{s}'|^3} d\mathbf{s}' + \int_{V\setminus\Omega} \frac{\rho_f(\mathbf{r}')(\mathbf{r}-\mathbf{r}')}{4\pi\epsilon_0\epsilon_m|\mathbf{r}-\mathbf{r}'|^3} d\mathbf{r}'\,. \tag{30}$$

The first term on the right-hand side of (30) represents the contribution from all surface charge at $\mathbf{s}' \neq \mathbf{r}$ and the second term originates from all free charge not at the surfaces (i.e., located in the embedding medium). The fields $\mathbf{E}_{pol}$ and $\mathbf{E}_f$ are evaluated at each surface point.

To solve (26) numerically, we discretize the interfaces into M finite boundary elements and transform it into a matrix equation. Since $\mathscr{A}_s$ has been shown to be well-conditioned [41,25], this method of finding the polarization charge distribution is more suitable than alternative approaches. Direct solution of the matrix form of (26) requires costly [$\sim\mathscr{O}(M^3)$] matrix inversion. This inversion needs to be repeated whenever the dielectric geometry changes—e.g., in each time step in a MD simulation of dielectric objects—and even for static dielectric geometries the solution involves dense matrix–vector multiplication at cost $\mathscr{O}(M^2)$. A far more efficient technique is the use of an iterative solver, for which we select GMRES [40]. GMRES only involves *fast* matrix–vector products, and aims to minimize the norm of the residual of (26),

$$\begin{aligned} r &= b_s - \mathscr{A}_s\sigma_{pol} \\ &= \sigma_f - \bar{\epsilon}_i(\sigma_f + \sigma_{pol}) - \epsilon_0\Delta\epsilon_i(\mathbf{E}_f + \mathbf{E}_{pol})\cdot\hat{\mathbf{n}}\,, \end{aligned} \tag{31}$$

where $\mathbf{E}_f + \mathbf{E}_{pol}$ is the *total* electric field at each surface patch, which can be computed directly with a fast Ewald solver. Thus, for a system containing M boundary elements and N isolated free charges, the residual can be obtained at a cost $\mathscr{O}((M+N)\log(M+N))$ for PPPM [42,43] or even $\mathscr{O}(M+N)$ for the fast multipole method (FMM) [56–59]. In practical MD simulations, once convergence has been attained in the first time step, subsequent time steps require less than 4 iterations to obtain the surface charge density with a relative error smaller than 10^{-4} [25,12]. An additional advantage of computing the electric field via Ewald summation is that periodic images are automatically taken into account, as is customary for simulations of electrostatic systems in bulk geometries.

We note that several additional considerations affect the accuracy and convergence rate. For boundary elements of finite size and nonzero curvature, surface charge within an element contributes to the normal component of the electric field and thus to the polarization charge. To first approximation, this has been taken into account via a "curvature correction." We approximate the correction term by assuming disk shaped patches with mean curvature, which works well for the spherical colloidal system in this paper [60,35]. Higher-order corrections can be applied as well [25, Sec. IV.B]. More sophisticated treatments via numerical quadrature are discussed in [61,41,62]. An alternative approach is the so-called "qualocation" method, which has been found to yield similar accuracy [63]. We further improve the convergence rate by constraining the net charge on dielectric objects per Gauss's law [25, Sec. IV.H].

3. Image-charge method

If all $\mathscr{P}$ dielectric objects $\mathscr{S}_i$ are of spherical shape, then an alternative method to the BEM is the ICM. In the BEM, polarization is characterized by the surface bound charge and the main objective is to efficiently obtain the bound charge density σ_{pol}. Once this is known, calculations are reduced to simple Coulomb summations according to (5). By contrast, in the ICM we instead solve the Poisson equation (14) with discontinuous coefficient by constructing an image-charge representation of $\widetilde{G}_{pol}$ in the presence of multiple dielectric spheres. Once $\widetilde{G}_{pol}$ is known, we can easily obtain the solution of (14) according to (16).

We start with a single dielectric sphere (i.e., $\mathscr{P}=1$) of radius a and relative permittivity ϵ_1. In this case, the exact $\widetilde{G}_{pol}$ has been obtained both by using spherical harmonics [64,65] (also known as the Kirkwood series) and by using the ICM [27]. Here we follow the latter approach. Consider a unit source charge located at $\mathbf{r}_s = (r_s,\theta_s,\phi_s) \in V\setminus\Omega$, expressed in spherical coordinates with respect to the center of the sphere. The polarization potential at any position $\mathbf{r} = (r,\theta,\phi)$ outside the sphere can be written as the sum of contributions from a Kelvin image $q_K = -\gamma a/r_s$ inside the sphere at the inversion point $\mathbf{r}_K = \mathbf{r}_s a^2/r_s^2$ and a line image charge distributed along $\mathbf{x} = x\mathbf{r}_s/r_s$ with $x \in [0, r_K]$,

$$\widetilde{G}_{pol}(\mathbf{r},\mathbf{r}_s) = \frac{q_K}{4\pi\epsilon_0\epsilon_m|\mathbf{r}-\mathbf{r}_K|} + \int_0^{r_K} \frac{q_{line}(x)}{4\pi\epsilon_0\epsilon_m|\mathbf{r}-\mathbf{x}|}dx\,, \tag{32}$$

where the line-charge density is given by

$$q_{line}(x) = \frac{\gamma\lambda}{a}\left(\frac{r_K}{x}\right)^{1-\lambda}\,. \tag{33}$$

Here $\gamma = (\epsilon_1 - \epsilon_m)/(\epsilon_1 + \epsilon_m)$ and $\lambda = \epsilon_m/(\epsilon_1 + \epsilon_m)$. After the first formulation of this line image-charge representation of the polarization potential by Neumann in the 19th century [27, pp. 279–282], it was rediscovered several times in various application areas; see [28] for a summary.

In MC or MD simulations, the integral over the line charge in (32) is evaluated numerically. However, due to the positive exponent $1-\lambda$ in (33), the line integral has an integrable power-law singularity at $x = 0$. Thus, conventional Gaussian quadrature fails to provide high accuracy, especially when $\lambda \to 0$. This singularity can be removed by setting $x = r_K(\frac{1-s}{2})^{1/\lambda}$, which yields

$$\int_0^{r_K} \frac{q_{\text{line}}(x)}{4\pi\epsilon_0\epsilon_m|\mathbf{r}-\mathbf{x}|}dx = \int_{-1}^{1} \frac{\gamma a}{8\pi\epsilon_0\epsilon_m r_s|\mathbf{r}-\mathbf{r}_K(\frac{1-s}{2})^{1/\lambda}|}ds \equiv \int_{-1}^{1} f(s)ds\,. \tag{34}$$

Thus, the $(L-1)$-point Gauss–Legendre quadrature can be used to approximate the line integral, resulting in a total of L image charges for the polarization potential,

$$\widetilde{G}_{\text{pol}}(\mathbf{r},\mathbf{r}_s) = \sum_{l=1}^{L} \frac{q_l}{4\pi\epsilon_0\epsilon_m|\mathbf{r}-\mathbf{x}_l|}\,, \tag{35}$$

where $q_1 = q_K$, $\mathbf{x}_1 = \mathbf{r}_K$ are the strength and position of the Kelvin image charge, $q_l = \omega_l\frac{\gamma a}{2r_s}$, $\mathbf{x}_l = \mathbf{r}_K\left(\frac{1-s_l}{2}\right)^{1/\lambda}$ for $l = 2, 3, \ldots, L$ the strengths and positions of the $(L-1)$ discrete point charges approximating the line charge, and the coefficients $\{\omega_l, s_l\}$ $(l = 2, 3, \ldots, L)$ are the $(L-1)$-point weights and locations on the interval $[-1, 1]$. The multiple-image approximation (35) was first proposed in [66], where it was combined with the FMM to achieve linear scaling. Later, it was applied to MC simulation of salt near a dielectric sphere [23].

Eq. (35) usually converges very rapidly when $\epsilon_1/\epsilon_m \lesssim 1$, so L can be small. For the limit $\lambda \to 1$ an alternative approach has been proposed, where the integral in (32) is performed analytically [22]. Evaluation of the potential then involves even fewer terms, although the term resulting from the line charge now involves a logarithm, so that efficient Ewald solvers cannot be used directly. On the other hand, when $\epsilon_1/\epsilon_m \gg 1$, i.e., the exponent $1/\lambda \gg 1$ in $f(s)$, the integrand becomes nearly singular at $s = -1$. One way to handle this is through subdivision and application of Gaussian quadrature to each subdivided interval. Whereas this may improve accuracy, it comes at a computational cost. As an alternative, we observe that the dielectric sphere approaches the conducting limit when $\epsilon_1/\epsilon_m \gg 1$. Since for a conducting sphere the image charges reduce to a Kelvin image charge plus a point charge $-q_K$ at the center of the sphere, in this limit we can simply place a point charge q_K at the sphere center to cancel the singularity,

$$\begin{aligned}\int_0^{r_K} \frac{q_{\text{line}}(x)}{4\pi\epsilon_0\epsilon_m|\mathbf{r}-\mathbf{x}|}dx &= \frac{\gamma\lambda}{4\pi\epsilon_0\epsilon_m a} r_K^{1-\lambda} \\ &\quad\times\left[\int_0^{r_K}\left(\frac{1}{x^{1-\lambda}|\mathbf{r}-\mathbf{x}|} - \frac{1}{x^{1-\lambda}r}\right)dx + \int_0^{r_K}\frac{1}{x^{1-\lambda}r}dx\right] \\ &= \frac{\gamma\lambda}{4\pi\epsilon_0\epsilon_m a} r_K^{1-\lambda}\int_0^{r_K}\left(\frac{1}{x^{1-\lambda}|\mathbf{r}-\mathbf{x}|} - \frac{1}{x^{1-\lambda}r}\right)dx - \frac{q_K}{4\pi\epsilon_0\epsilon_m r} \\ &\equiv \int_0^{r_K} g(x)dx - \frac{q_K}{4\pi\epsilon_0\epsilon_m r}\,.\end{aligned} \tag{36}$$

As before, the integral $\int_0^{r_K} g(x)dx$ can then be handled with $(L-2)$-point Gauss–Legendre quadrature, again yielding L image charges for the polarization potential

$$\widetilde{G}_{\text{pol}}(\mathbf{r},\mathbf{r}_s) = \sum_{l=1}^{L} \frac{q'_l}{4\pi\epsilon_0\epsilon_m|\mathbf{r}-\mathbf{x}'_l|}\,. \tag{37}$$

Here $q'_1 = q_K$ and $\mathbf{x}'_1 = \mathbf{r}_K$ represent the Kelvin image charge, whereas

$$q'_l = \omega'_l\frac{\gamma\lambda}{a}\left(\frac{r_K}{s'_l}\right)^{1-\lambda}, \quad x'_l = s'_l \quad (l = 2, 3, \ldots, L-1) \tag{38}$$

$$q'_L = -\sum_{l=2}^{L-1}\omega'_l\frac{\gamma\lambda}{a}\left(\frac{r_K}{s'_l}\right)^{1-\lambda} - q_K\,, \quad x'_L = 0 \tag{39}$$

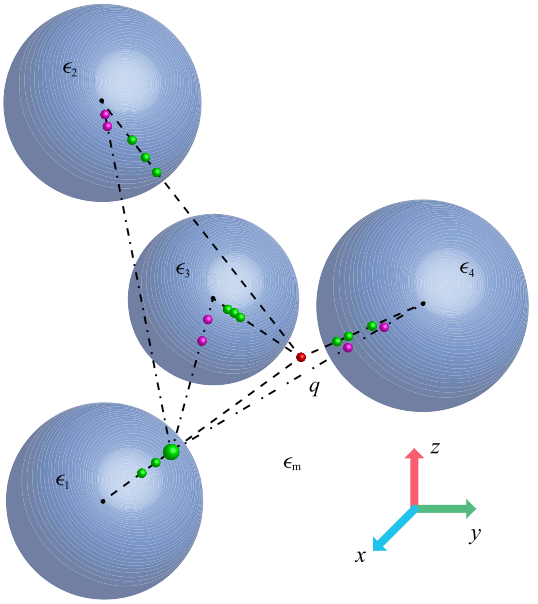

Fig. 1. Construction of image charges by reflections between dielectric spheres (blue). A source charge q located in the exterior region induces L_1 first-level image charges (green spheres, here $L_1 = 3$) inside each sphere. Subsequently, each first-level image induces L_2 second-level images inside all other spheres. In this example $L_2 = 2$ and only the images for the enlarged first-level image are shown (purple spheres). This reflection procedure is performed recursively until convergence is reached. (For interpretation of the references to color in this figure legend, the reader is referred to the web version of this article.)

are the strengths and positions of the $(L-1)$ discrete point charges approximating the line-charge integral (36). The coefficients $\{\omega_l', s_l'\}$ $(l = 2, 3, \ldots, L-1)$ are the $(L-2)$-point weights and locations on the interval $[0, r_K]$. The quadrature schemes (35) and (37) are appropriate for $\epsilon_1/\epsilon_m \lesssim 1$ and $\epsilon_1/\epsilon_m \gg 1$, respectively. In the model investigated in Sections 5 and 6, the dielectric ratio is $\epsilon_1/\epsilon_m = 0.025$, so (35) is used.

When $\mathscr{P} > 1$, the polarization potential can be constructed by a procedure of iterative image-charge reflections [67,31], as illustrated in Fig. 1. If a unit charge is located at $\mathbf{r}_s$ in the exterior region $V\backslash\Omega$, then L_1 image charges are produced in each sphere according to the one-sphere formulation (35) or (37). The unit charge together with the set of L_1 images in sphere $\mathscr{S}_i$ generate an electric field that satisfies the boundary condition (23) on the surface $\partial\mathscr{S}_i$. To satisfy the boundary conditions on the other surfaces $\partial\mathscr{S}_j (j \neq i)$, L_2 additional (second-level) image charges are generated in $\mathscr{S}_j (j \neq i)$ for each of the L_1 image charges in $\mathscr{S}_i$. Recursive iteration of this procedure yields the polarization potential [31],

$$\widetilde{G}_{\mathrm{pol}}(\mathbf{r}, \mathbf{r}_s) = \frac{1}{4\pi\epsilon_0\epsilon_m} \sum_{n_1=1}^{\mathscr{P}} \sum_{l_1=1}^{L_1} \left\{ \frac{q_{n_1}^{l_1}}{|\mathbf{r} - \mathbf{x}_{n_1}^{l_1}|} + \sum_{\substack{n_2=1 \\ n_2 \neq n_1}}^{\mathscr{P}} \sum_{l_2=1}^{L_2} \left[\frac{q_{n_2 n_1}^{l_2 l_1}}{|\mathbf{r} - \mathbf{x}_{n_2 n_1}^{l_2 l_1}|} + \sum_{\substack{n_3=1 \\ n_3 \neq n_2}}^{\mathscr{P}} \sum_{l_3=1}^{L_3} \left(\frac{q_{n_3 n_2 n_1}^{l_3 l_2 l_1}}{|\mathbf{r} - \mathbf{x}_{n_3 n_2 n_1}^{l_3 l_2 l_1}|} + \cdots \right) \right] \right\}. \tag{40}$$

Here q and $\mathbf{x}$ with superscripts $l_i l_{i-1} \cdots l_1$ and subscripts $n_i n_{i-1} \cdots n_1$ are the next-level image charges of the charges with indices $l_{i-1} \cdots l_1$ and $n_{i-1} \cdots n_1$. Their strengths and locations are determined according to the one-sphere formulation. Eq. (40) generalizes the result of [31] by introducing a variable number of image charges at different levels, permitting optimization of the parameters L_i. If we estimate $\widetilde{G}_{\mathrm{pol}}$ by truncating (40) at reflection level R, the number of image charges $\mathscr{I}$ for each source charge is

$$\mathscr{I} = \mathscr{P} \sum_{i=1}^{R} \left[(\mathscr{P} - 1)^{i-1} \prod_{j=1}^{i} L_j \right]. \tag{41}$$

Thus $\mathscr{I}$ increases exponentially with R. Fortunately, the truncation error in $\widetilde{G}_{\mathrm{pol}}$ decreases rapidly [67,31] (see also Appendix A.1). Moreover, analysis of the quadrature error (Appendix A.2), shows that for higher reflection levels $i > 1$, L_i may be reduced without loss of accuracy. Finally, since the polarization energy now is comprised of Coulombic interactions between image and source charges, it can be evaluated via fast algorithms such as the FMM [56–59] or treecode algorithms [44–46].

Although the ICM avoids the need to calculate surface bound charge, it can be obtained directly once the electrostatic potential in the exterior region $\Phi_{\mathrm{out}}(\mathbf{r})$ or the electric field has been computed from the free and image charges. This explicit

evaluation is useful, e.g., for comparison with the BEM. If $\mathbf{E}_{\text{out}}(\mathbf{r})$ denotes the electric field in the exterior region (relative permittivity ϵ_{m}), then the normal component of this field at position $\mathbf{r}$ on an interface with a dielectric object (relative permittivity ϵ_i) is

$$\mathbf{E}_{\text{out}}(\mathbf{r}) \cdot \hat{\mathbf{n}} = -\frac{\partial \Phi_{\text{out}}(\mathbf{r})}{\partial n} , \tag{42}$$

where $\hat{\mathbf{n}}$ is the outward normal. The normal component of the *interior* electric field in the dielectric, at the same surface position, then follows from (23) and can be substituted in (24) to obtain the bound charge density

$$\sigma_{\text{pol}}(\mathbf{r}) = \frac{1}{\epsilon_i}\left[(\epsilon_i - \epsilon_{\text{m}})\epsilon_0 \mathbf{E}_{\text{out}}(\mathbf{r}) \cdot \hat{\mathbf{n}} - (\epsilon_i - 1)\sigma_{\text{f}}(\mathbf{r})\right] . \tag{43}$$

We illustrate this with a practical example in Section 5.3.

4. Efficiency comparison

To compare the computational complexity of both methods, we consider geometries that are amenable to both approaches, e.g., configurations of spheres. Even though the efficiency will depend on implementation and also on the physical system considered, general observations can be made. Specifically, the computational cost of both methods is dominated by the electrostatic solver and hence determined by the total number of charges that contribute to the electrostatic potential.

Consider a system of N free point charges placed outside $\mathscr{P}$ neutral spherical dielectric objects. In the BEM, if a total of M surface elements are required to achieve a certain accuracy, the total number of charges is $N + M$. For the PPPM method employed in [25,12], the computational cost of a single time step is thus $\mathscr{O}((N+M)\log(N+M))$, although (as noted in [25]) the FMM may be better suited to the nonuniform distributions typical of the BEM. For dielectric systems containing objects of similar size, $M \propto \mathscr{P}$, so that the BEM has a nearly linear dependence on both the number of source charges N and the number of dielectric object $\mathscr{P}$. It must be noted, however, that M may have to be increased if point charges approach a dielectric interface very closely, or if multiple dielectric objects aggregate. In addition, we remark that in each time step GMRES typically requires 4 evaluations of the electrostatic potential to reach convergence.

For the ICM, the same system consists of N source charges and $N\mathscr{I}$ image charges. In the Barnes–Hut octree algorithm [44–46], the computational complexity of an MC cycle scales as $\mathscr{O}(N\mathscr{I}\log(N\mathscr{I}))$ [68]. Not only does $\mathscr{I}$ increase as a power law of $\mathscr{P}$, cf. (41), it also is comparable in magnitude to M (see Section 5.2). However, whereas for the BEM it appears additive to N in the computational cost, for the ICM it appears multiplicatively. Thus, for large N or $\mathscr{P}$, the BEM generally outperforms the ICM. An important advantage of the ICM, on the other hand, is that geometric singularities are naturally avoided, as it employs a closed-form expression for the Green's function. In addition, the number of image charges in the ICM does not depend on the colloidal size, making it advantageous for the simulation of large colloids. Moreover, the efficiency can be increased by dynamically tuning $\mathscr{I}$ based upon the geometry, e.g., when dielectric objects are spaced far apart or source charges are not close to an object. Also, since the image charges are distributed nonuniformly within the spheres, the computational cost can be reduced by decreasing the number of clusters in the Barnes–Hut octree algorithm.

If the dielectric objects have arbitrary (nonuniform) surface charge density, no additional computational expense is incurred in the BEM, as this charge can be distributed across the boundary patches. On the other hand, in the ICM this surface discretization is generally costly, as it increases the number of source charges. For immobile objects, the potential generated by these charges and their image charges is constant and can be precomputed within a simulation, but for dynamic dielectric objects this is not the case.

As a concrete comparison between the BEM and ICM we consider the system of two colloids immersed in an electrolyte, described in Section 6 below (all technical parameters are described there as well). We determine the time it takes to obtain an independent sample for the net force on one of the colloids from the integrated autocorrelation time [69]. Using the BEM, this requires 120 MD time steps, corresponding to 45 seconds of CPU time (Intel Xeon E5-2620 v3, 2.40 GHz). When interpreting this time requirement, it is important to note that the system contains $N = 702$ ions as well as $M = 2944$ surface elements. On the other hand, in the ICM an independent sample is obtained after every 1000 MC cycles, where a cycle corresponds to one proposed move per ion (on average). For the parameter choice adopted in Section 6 ($\mathscr{I} = 310$ image charges, reflection level "5332" as described in Section 5.2) this corresponds to 50 seconds of CPU time, although this can be reduced to 40 seconds by choosing $\mathscr{I} = 248$ image charges (reflection level "4332") while retaining a sufficient precision, cf. Section 5.2. In comparing these numbers, it should be noted that the cylindrical simulation cell adopted for the ICM contains only 276 ions, 2.5 times less than the periodic cell employed in the BEM (the larger cell in the BEM is chosen to avoid artificial periodicity effects). A final practical point is that the net force follows directly in the MD simulation, whereas relatively costly numerical differentiation [Eq. (49)] is required in the MC simulation. Given the slow decorrelation of the system it is important to avoid performing this derivative unnecessarily often.

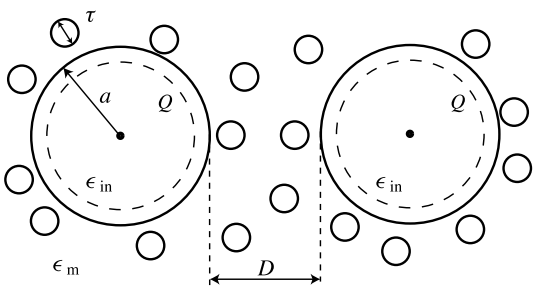

Fig. 2. Two-dimensional illustration of the so-called primitive model of two dielectric colloids surrounded by an electrolyte.

5. Numerical results: static configurations

5.1. Model setup

To test the performance of these two algorithms, we apply them to a system of two dielectric colloids immersed in an electrolyte (Fig. 2). The solvent is treated implicitly as a dielectric continuum with relative permittivity ϵ_{m} and the colloids and ions are represented explicitly by spheres with a soft repulsive potential. The colloidal particles ("macroions") have radius a and are placed at a surface-to-surface separation D. They both carry a total free charge $Q = Ze$ distributed uniformly on their surface and have an internal dielectric constant ϵ_{in}. The ions are of diameter τ with charge $q = ze$ and are considered non-polarizable, although their effective charge is reduced by a factor $1/\epsilon_{\mathrm{m}}$ due to polarization of the surrounding medium.

The potential energy of the system V_{tot} can be expressed as a sum of three contributions

$$V_{\mathrm{tot}} = V_{\mathrm{LJ}} + V_{\mathrm{Coul}} + V_{\mathrm{pol}} \,, \tag{44}$$

where V_{LJ} represents the non-electrostatic repulsions, V_{Coul} the pairwise electrostatic interactions between the free charges, and V_{pol} the polarization energy arising from the interactions involving bound charges. The repulsive interaction between any two particles i and j is modeled via a shifted-truncated Lennard–Jones (LJ) potential

$$\beta u_{\mathrm{LJ}}(r_{ij}) = \begin{cases} \infty & \text{if } r_{ij} \le \Delta_{ij} \\ 4\left[\left(\frac{c}{r_{ij}-\Delta_{ij}}\right)^{12} - \left(\frac{c}{r_{ij}-\Delta_{ij}}\right)^{6}\right] + 1 & \text{if } \Delta_{ij} < r_{ij} < \Delta_{ij} + 2^{\frac{1}{6}}c \\ 0 & \text{if } r_{ij} \ge \Delta_{ij} + 2^{\frac{1}{6}}c \end{cases} \,, \tag{45}$$

where $\beta = 1/(k_{\mathrm{B}}T)$ is the inverse thermal energy (with k_{B} Boltzmann's constant and T the absolute temperature), r_{ij} the distance between the particle centers, and $\Delta_{ij} = (d_i + d_j)/2 - c$ the hard-core distance. Here, d_i and d_j are the diameters of particles i and j, respectively, and c is set to be the diameter of the mobile ions, $c = \tau$. Thus, at contact ($D = 0$, $r = 2a = d_{\mathrm{M}}$) the two colloids have a repulsive Lennard–Jones interaction energy $u_{\mathrm{LJ}} = k_{\mathrm{B}}T$. To avoid the singularity that would arise if the position of an ion would coincide with a surface element, the surface elements are placed at the divergence of the sphere–ion shifted-truncated LJ potential, i.e., at a radius $a - \tau/2$, indicated by the dashed circles in Fig. 2.

The central force $F_{\mathrm{tot}}(D) = -\partial V_{\mathrm{tot}}/\partial D$ between the two colloids thus comprises two contributions

$$F_{\mathrm{tot}}(D) = F_{\mathrm{LJ}}(D) + F_{\mathrm{ele}}(D) \,, \tag{46}$$

where we only consider the component parallel to their center-to-center axis, and $F_{\mathrm{LJ}}(D)$ is the force originating from the LJ interactions and $F_{\mathrm{ele}}(D)$ the electrostatic force. Whereas the former is straightforward to obtain, the evaluation of $F_{\mathrm{ele}}(D)$ is nontrivial. As derived in [25] by differentiation of the total energy, the total electrostatic force on a rigid dielectric object $\mathscr{S}_i$ is

$$F_{\mathrm{ele}}(D) = \int_{\mathscr{S}_i} f'(\mathbf{r}) d\mathbf{r} \,, \tag{47}$$

where $f'(\mathbf{r})$ is the parallel component of

$$\mathbf{f}(\mathbf{r}) = \epsilon_{\mathrm{m}} \left[\rho_{\mathrm{f}}(\mathbf{r}) + \rho_{\mathrm{pol}}(\mathbf{r})\right] \mathbf{E}(\mathbf{r}) \,, \tag{48}$$

In the BEM-based calculations, we thus compute the total electrostatic force via summation over all boundary elements.

On the other hand, when using the ICM, we evaluate $F_{\mathrm{ele}}(D)$ through numerical differentiation of the energy,

$$F_{\mathrm{ele}}(D) \approx -\frac{V_{\mathrm{ele}}(D + \delta D) - V_{\mathrm{ele}}(D)}{\delta D} \,. \tag{49}$$

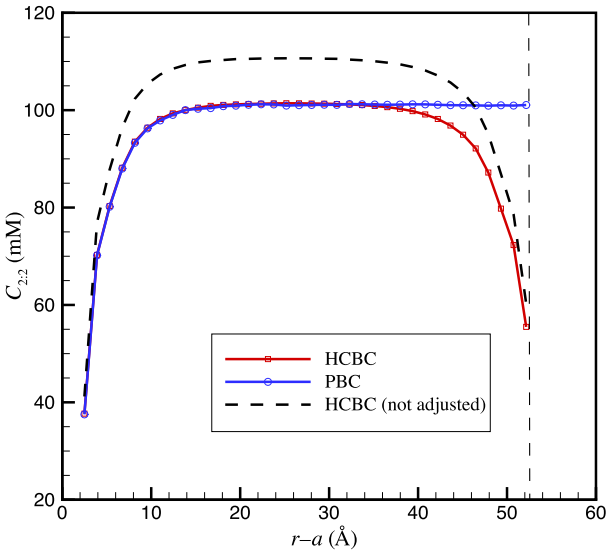

Fig. 3. Comparison of the radial distribution of divalent ions around an isolated dielectric colloid (radius $a = 20$ Å) placed in a periodic box of linear size 180 Å ("PBC") and in a spherical cell (radius 72.65 Å) with hard-core boundary conditions ("HCBC"). Whereas the periodic box shows a constant salt concentration away from the colloidal surface, the system with the spherical hard wall exhibits significant depletion of salt near the wall (location marked by the dashed vertical line), which in turn gives rise to a spurious increase of the bulk concentration [indicated by the curve "HCBC (not adjusted)"]. To account for this effect, we adjust the number of ions such that both systems have the same effective bulk salt concentration (curve "HCBC").

For a given configuration, we first evaluate the total electrostatic energy $V_{\text{ele}} = V_{\text{Coul}} + V_{\text{pol}}$, and then displace one colloid by δD along the vector connecting the centers of the two colloids. Since this entails a change in $\epsilon(\mathbf{r})$, recalculation of V_{ele} requires the reconstruction of all image charges. For the system specified below, we choose $\delta D = 2 \times 10^{-5}$ Å.

In the numerical comparisons presented here, we set the solvent conditions to represent water at room temperature, i.e., $T = 298$ K and $\epsilon_{\text{m}} = 80$, resulting in a Bjerrum length $\ell_{\text{B}} = e^2/(4\pi\epsilon_0\epsilon_{\text{m}}k_{\text{B}}T) = 7.14$ Å. The colloids have dielectric constant $\epsilon_{\text{in}} = 2$ and diameter $d_{\text{M}} = 40$ Å. The electrolyte consists of $C_{\text{s}} = 100$ mM 2:2 salt (ion diameter $\tau = 4.5$ Å), which corresponds to a Debye length $\ell_{\text{D}} = \sqrt{\epsilon_0\epsilon_{\text{m}}k_{\text{B}}T/(8C_{\text{s}}e^2)} = 4.81$ Å. We focus on dielectric effects by choosing $Q = 0$ (or, equivalently, $\sigma_{\text{f}} = 0$), so that the electrostatic force acting on the two colloids arises solely from the interactions of the polarization charge induced on either colloid with the salt ions and with the induced charge on the other colloid. We choose divalent salt, since the dielectric forces scale as z^2.

For calculations involving the ICM we employ a cylindrical cell [70], where the ions are confined by hard walls (both the cylindrical shell and its top and bottom), such that an ion acquires infinite energy if its center is moved outside of the cylinder. The colloids are fixed on the cylinder axis, while the mobile ions can move freely within the cylinder. The cylinder radius (65 Å) and length (190 Å) are chosen to be much larger than the Debye screening length. For the BEM we instead employ a cubic, periodically replicated box. In Section 5.2, we use configurations that are produced by the ICM, but for the comparison calculations performed with the BEM we place these configurations (which contain 300 ions) in a box of much larger volume (linear dimension 4500 Å) than the cylindrical cell, to suppress effects of the periodic boundary conditions. On the other hand, for the equilibrium results in Section 6 we find that the cylindrical volume suffers from significant boundary effects. Ions near the cylinder walls lack a symmetric shell of screening counterions, which in turns leads to a depletion of ions at the wall [71]. Fig. 3 illustrates this effect for a spherical cell. If the number of ions is not adjusted to account for this effect, the concentration in the remainder of the cylinder will be significantly *increased*, hindering an accurate comparison with the BEM results. In the BEM we realize a salt concentration of 100 mM by placing 702 ions in a box of linear dimension 180 Å, which due to the excluded volume of the colloids results in an effective (bulk) concentration of ∼101 mM. On the other hand, in the ICM we must reduce the number of ions from 300 to 276 to achieve the same concentration in the bulk, as confirmed in Fig. 3 for the spherical system. Whereas it also would have been possible to eliminate this effect via an attractive surface potential, we demonstrate in Section 6 that a proper bulk salt concentration surrounding the colloids is sufficient to reproduce the correct mean colloidal force.

5.2. Parameter dependence for the BEM and the ICM

We first examine the accuracy of both methods as a function of parameter choice (surface discretization for the BEM and number of images and level of reflection for the ICM). For each of 14 surface separations D (3–16 Å, in steps of 1 Å) we perform a simulation of the system described above (cylindrical cell, 300 ions) to produce 100 independent configurations corresponding to thermodynamic equilibrium. For each of these configurations, we then compute the force on one of the

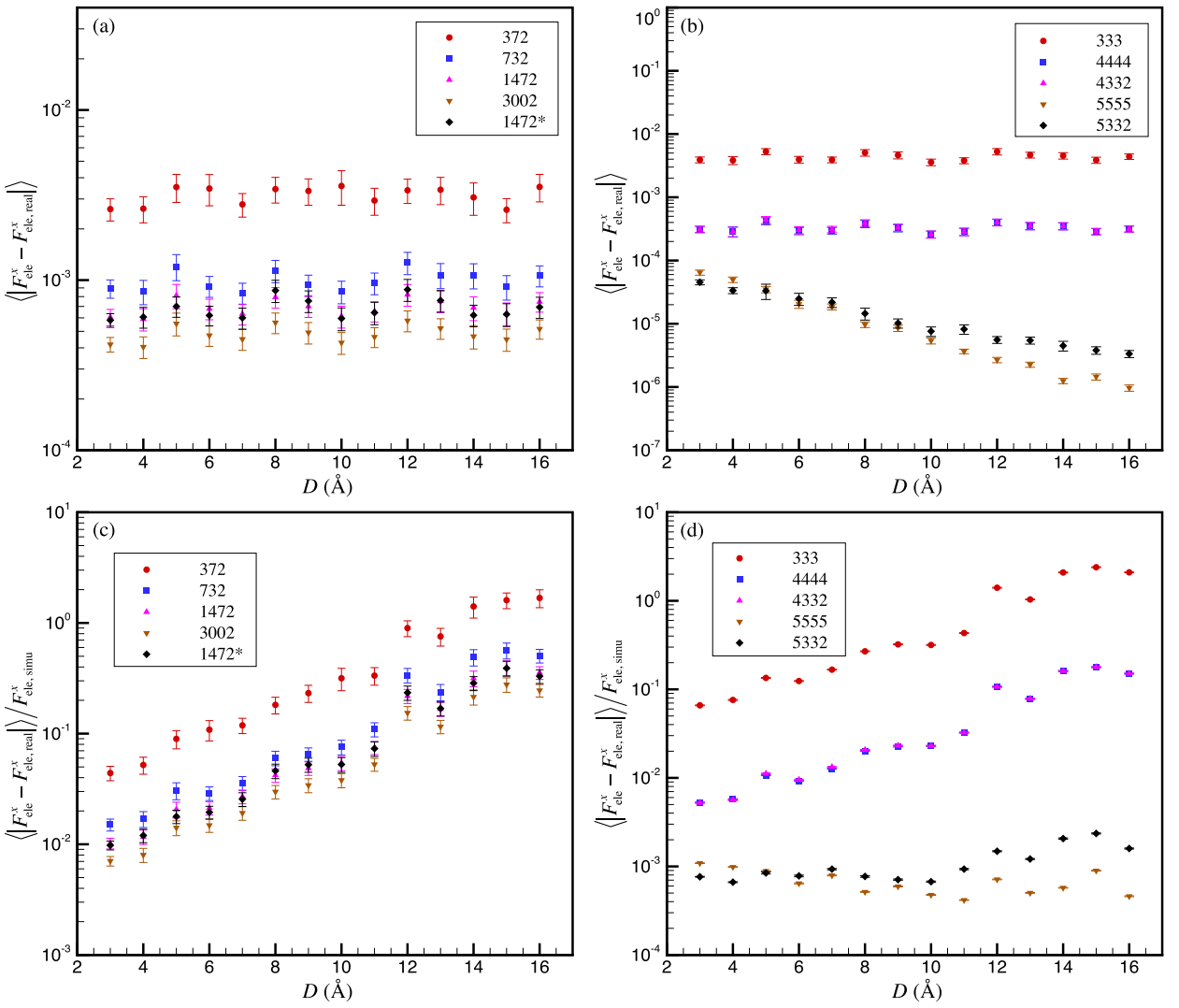

Fig. 4. Accuracy of the electrostatic force between two neutral colloids immersed in an electrolyte, as a function of surface separation, $D = 3$–16 Å. Physical parameters are described in the main text. Panels (a) and (b) show the ensemble-averaged absolute error in the component of the absolute force along the center-to-center axis between the colloids for (a) the BEM at different surface discretizations (numbers in the key indicate the number of surface elements per sphere) and (b) the ICM at different reflection levels R and numbers of image charges L_i (numbers in the key indicate the number of image charges per reflection level). It is important to note that these estimates significantly *overestimate* the error obtained in a typical simulation, by averaging the absolute values of the deviations. Panels (c) and (d) show the same data as panels (a) and (b), respectively, but normalized by the magnitude of the force obtained in the simulations of Section 6 (electrostatic force in Fig. 6a). The increase of these relative uncertainties with increasing D simply reflects the fact that the induced forces become very small at larger colloid separations. The exception to this trend are the ICM data [panel (d)] for the "5332" and "5555" parameters; here the relative deviation remains mostly flat since the effect of the decreasing force is partly negated by the decrease in the truncation error with increasing D [cf. panel (b) and derivation in Appendix A.1]. Force unit is $k_B T/\ell_B$. Ensemble averages are obtained from 100 independent equilibrium configurations, where the same set of configurations is employed for the BEM and ICM calculations.

colloids using the ICM with $L = 5$, $R = 6$ and direct pairwise summation. These parameters yield an absolute accuracy of 10^{-7} and the results serve as the reference values.

Fig. 4 shows, for each separation D, the absolute error in the force on a single colloid averaged over the 100 configurations as computed with the BEM and ICM for various parameter choices, along with the relative errors.

For the BEM we focus on the number of surface elements. Thus, we choose a sufficiently small convergence criterion for GMRES and high enough accuracy for the Ewald solver (relative error 10^{-4} for both GMRES and Ewald) to ensure that errors resulting from these two factors are small compared to the discretization error. As shown in Fig. 4(a), for systems with 372 to 3002 patches per colloid, the ensemble-averaged absolute errors in the forces are less than $0.003 k_B T/\ell_B$ for all 14 separations. Moreover, they decrease monotonically with increasing number of boundary elements, improving by an order of magnitude between the coarsest and the finest grids. We also investigate the role of the orientation of the surface grid [data labeled "1472*"]. Whereas all other grids are oriented such that for both colloids a grid point (center of

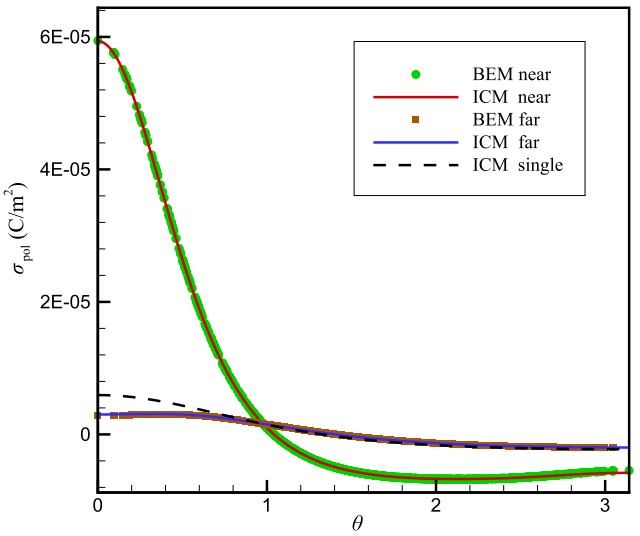

Fig. 5. Comparison of the BEM and the ICM for the surface bound charge density σ_{pol} induced by a monovalent positive ion at $x = 60$ Å on two colloids ($\epsilon_{\text{in}} = 2$) at $x = 21.5$ Å ("near") and $x = -21.5$ Å ("far") in water ($\epsilon_{\text{m}} = 80$). The azimuthal symmetry makes it possible to parametrize σ_{pol} by the polar angle θ between the positive x-axis and the surface points. The results from both methods are in excellent agreement. The curve labeled "ICM single" represents the bound charge density on the "far" colloid in the absence of the intervening "near" colloid, illustrating the screening effect of the latter.

a surface element) lies on their center-to-center axis, for "1472*" the grid is oriented such that this axis passes through the edge of a surface element. The grid orientation can have a significant effect in individual configurations, depending on whether an ion resides close to a surface element, but we find that such differences vanish in the ensemble averages, as expected. In practical simulations (Section 6), we employ 1472 surface elements per colloid, which yields an absolute error less than $10^{-3} k_{\text{B}}T/\ell_{\text{B}}$. We note that the absolute deviations provide an upper bound for the systematic errors incurred in the simulations. Fig. 4(c) shows the same data as panel (a), but normalized by the magnitude of the force. As this force becomes small when D increases, the relative deviations display an increasing trend.

Figs. 4(b) and (d) show the absolute deviations in the force as well as the relative values of these errors for the same configurations as employed in panels (a) and (c), but now calculated by the ICM. To study the convergence of the polarization potential (40), we vary both the maximum reflection level R and the number of image charges L_i for each level. The different choices are labeled "$L_1 L_2 \cdots L_R$" and show a decrease in the absolute error by at least two orders of magnitude between "333" and "5555". Interestingly, the results in Fig. 4(b) show that the number of images at the higher reflection levels can be decreased without consequences for the accuracy, with excellent agreement between "4444" and "4332," and quite close agreement between "5555" and "5332". This approach can significantly reduce the computational cost. For example, "5332" requires $\mathscr{I} = 310$ image charges per source charge (ion), five times less than "5555" ($\mathscr{I} = 1560$). The decreasing error with increasing D in panel (b) arises from the decreasing truncation error, see Appendix A.1.

5.3. Induced surface charge density

It is instructive to compare the polarization charge as computed by the BEM and the ICM. We center the two spherical colloids at $(\pm 21.5, 0, 0)$ Å (i.e., at a surface separation $D = 3$ Å), and place a single positive monovalent ion at $(60, 0, 0)$ Å. Even this simple configuration is not easy to treat analytically, due to the interaction between polarization charges on different spheres. For both colloids, we determine σ_{pol} as a function of the polar angle θ. In the BEM, we use 1472 surface elements per colloid. For the ICM, we use "5555" [i.e., $R = 4$ and $L_i = 5$ $(i = 1, \ldots, 4)$] and exploit (43) to determine σ_{pol} for arbitrary θ. As shown in Fig. 5, the results obtained by both methods are in excellent agreement.

We note some interesting physical aspects of the induced polarization. Since the permittivity of the colloids ($\epsilon_{\text{in}} = 2$) is lower than of the surrounding medium ($\epsilon_{\text{m}} = 80$), positive bound charge accumulates near $\theta = 0$, i.e., the region facing the ion. This positive charge is then compensated by a gradually varying negative bound charge density over the rest of the colloidal surfaces, such that the neutrality condition is satisfied for the total bound charge on each colloid. In the BEM, we also constrain the net bound charge to be zero after each iteration to facilitate convergence and accuracy. In addition, σ_{pol} for the "far" sphere (positioned on the negative x-axis) has much lower bound charge density than the "near" sphere (positioned on the positive x-axis). This is not only due to its larger distance from the ion, but also due to the screening effect of the bound charges on the "near" sphere, which can be approximated as a dipole with its dipole moment pointing towards the positive source charge, partially canceling the source charge field. This is confirmed by the curve labeled "ICM single" in Fig. 5, which shows the surface bound charge density on the sphere on the negative x-axis in the *absence* of the dielectric sphere on the positive x-axis. The induced charge density is then significantly higher, especially at small θ.

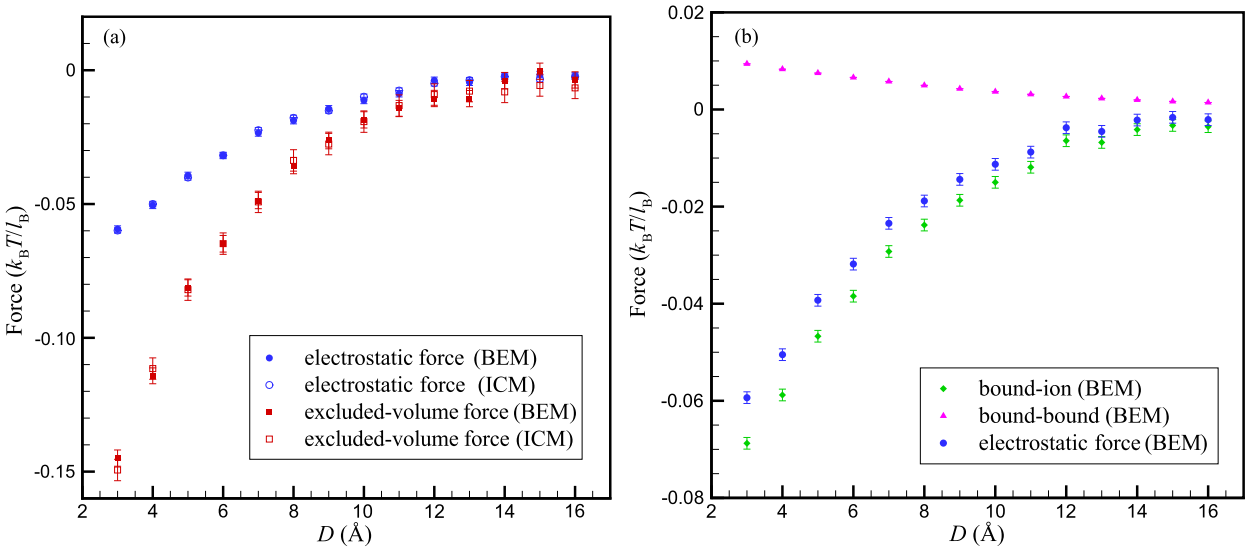

Fig. 6. Mean force between two neutral dielectric colloids induced by a divalent aqueous electrolyte (100 mM). BEM data are obtained via a MD simulation incorporating the boundary-element method, whereas the ICM data are calculated in a MC simulation with iteratively reflected image charges. (a) Mean electrostatic and excluded-volume force. Note that both forces are attractive and have a similar range. (b) Decomposition of the electrostatic force into an attractive contribution due to ion–bound charge forces (green diamonds) and a repulsive contribution due to the forces between bound charges induced on different colloids (purple triangles; error bars smaller than the symbol size). Note that the blue circles correspond to the same symbols as shown in panel (a), and represent the sum of the bound–bound forces and the bound–ion forces. (For interpretation of the references to color in this figure legend, the reader is referred to the web version of this article.)

6. Numerical results: thermodynamic equilibrium

Having verified the accuracy of both methods and the required parameter choices, we now proceed to evaluate their performance in practical simulations of thermodynamic properties. As a model system, we consider the ensemble-averaged force between two neutral dielectric colloids induced by a symmetric divalent aqueous electrolyte. As noted in (46), this force has two contributions: (i) the short-range excluded-volume repulsions that result in a depletion-type [72,73] force that is ultimately entropic in nature and (ii) an electrostatic contribution involving polarization charges induced by ions. The ensemble-average of even the first contribution is not easily obtained by other means, given that the ionic arrangements are influenced by ion–ion interactions as well as ion–polarization interactions, where the polarization charges in turn are determined by the ionic configurations. For the second contribution, already the force in a single sample, (47) and (48), requires careful consideration.

For the BEM, we perform MD simulations that start from 702 ions randomly arranged around the two colloids. We employ the velocity Verlet algorithm with a Langevin thermostat (damping parameter time $20t_0$, where $t_0 = (m\tau^2\beta)^{1/2}$ is the LJ unit time with τ the ion diameter and m the ion mass). The RMS relative error of the PPPM method is chosen to be $\mathcal{O}(10^{-4})$ with real space cutoff 4.0τ. Starting from a small time step (to remove particle overlaps) we gradually increase the time step to $0.3t_0$. After 6×10^4 time steps (corresponding to $3700t_0$ due to the varying time step size) we commence sampling and continue for 15×10^4 time steps ($45\,000t_0$). The electrostatic force on each of the colloids is sampled after every 150 steps, whereas the shifted-truncated LJ repulsions (which exhibit a large variance and decorrelate rapidly) are sampled 30 times more frequently. For each separation, we perform 200 independent runs, resulting in a total of 4×10^5 independent samples per separation for the electrostatic force and 1.2×10^7 samples for the depletion force.

The ICM is incorporated within canonical MC simulations employing single-particle moves with a maximum displacement ℓ_B, resulting in an acceptance rate ∼47%. To realize the efficiency of the Barnes–Hut octree algorithm for the evaluation of the energy change resulting from a single displacement, we use a tailored variant of the octree routine [47]. The treecode parameters are set to be MAC = 0.1 and $p = 3$, which guarantees a relative error of less than 1.4×10^{-5}. From a random configuration with 276 ions, we perform simulated annealing over 10^5 cycles (a single cycle corresponds to one move per particle on average), lowering the temperature from $T = 2100$ K to $T = 298$ K. After another 10^5 equilibration cycles, we continue for 10^7 production cycles (100 independent runs of 10^5 cycles per separation), sampling every full cycle. Per separation, this yields 5×10^4 independent samples for the electrostatic force and 2×10^6 samples for the depletion force. The force on one colloid is computed through numerical differentiation, Eq. (49).

Fig. 6(a) shows the mean electrostatic and excluded-volume force as a function of colloid surface separation. We choose $M = 2 \times 1472$ curved surface elements in the BEM and four levels of reflection ("5332") for the ICM, which has 310 image charges per ion (10 first-level images, 30 second-level, 90 third-level, and 180 fourth-level). We note that Fig. 4(b) indicates that already with parameter choice "4332" the ICM could have achieved an accuracy comparable to that of the BEM for 1472 patches per colloid, although this would have reduced the number of image charges by only 20%. For all separations

the BEM/MD and ICM/MC data agree within the statistical uncertainties. These results also demonstrate the importance of polarization effects in the induced colloidal attraction: The electrostatic force has a magnitude of around 40% of the excluded-volume forces. Using the BEM, we can easily decompose the polarization forces into interactions between bound charges residing on separate colloids and interactions between bound charges and ions [Fig. 6(b)]. We note that the time-averaged polarization charge vanishes, owing to the anion–cation symmetry of the salt. However, the instantaneous force of a bound charge on the ion that induces it is always repulsive, and this effect is stronger in the region between both colloids, as the ion there will experience a repulsive force from bound charges it induces on both colloids. This leads to a depletion of ions in this region, so that the average net ion–bound charge force between the colloids is *attractive*, reinforcing the depletion attraction induced by the excluded-volume interactions. On the other hand, the bound–bound interaction between the two colloids is repulsive for symmetry reasons.

7. Summary

We have reviewed two numerical approaches for solving the Poisson equation in systems with discontinuous dielectric constant, namely a method based upon image charges and a method based upon discretization of dielectric interfaces. Specifically, both methods are applied to systems comprised of multiple dielectric objects. The BEM can be applied to arbitrary geometries. The ICM avoids the need for surface discretization by exploiting a closed-form representation of the Green's function, but is restricted to assemblies of spherical objects. We have analyzed the computational complexity of both approaches and through direct comparison have demonstrated how, for a given accuracy, the number of image charges can be reduced at higher reflection levels. We have implemented both methods in particle-based simulations, the BEM within a MD simulation and the ICM within a MC simulation. As a practical demonstration, we have used these simulations to determine the salt-induced attractive effective force between two neutral dielectric colloidal particles.

Acknowledgements

Z.G. and Z.X. acknowledge support by the Natural Science Foundation of China under Grant Nos. 11101276 and 91130012, the Chinese Organization Department, and the HPC center of Shanghai Jiao Tong University. H.W. and E.L. acknowledge support by the U.S. National Science Foundation under Grant Nos. DMR-1310211 and DMR-1121262 at the Materials Research Center of Northwestern University.

Appendix A. Error analysis of the ICM in a limiting case

This appendix provides an error analysis of the polarization potential (40) calculated by the ICM. The total error is composed of the error E_{T} due to truncation of (40) at reflection level R and the Gaussian quadrature error E_{Q}, which is the sum of individual errors at each reflection level. Here, we estimate these errors for the self energy of a unit charge in the presence of two dielectric spheres. In dimensionless units, this is equivalent to analyzing $\Phi_{\mathrm{self}} = G_{\mathrm{pol}}(\mathbf{r}, \mathbf{r})$. The estimation of E_{T} follows [31] and is included here for completeness.

A.1. Truncation error

We place two dielectric spheres of radius a at $\mathbf{o}_1$ and $\mathbf{o}_2$, respectively, so that $r_{12} = |\mathbf{o}_1 - \mathbf{o}_2|$ is their center-to-center distance and $D = r_{12} - 2a$ their surface separation. We consider the extreme case in which the unit source charge is located at the midpoint of $\overline{\mathbf{o}_1\mathbf{o}_2}$. Any deviation from this point will lead to a faster convergence of the image-charge approximation, because at this point the higher-order image multipoles reduce to image dipoles. Thus, this case provides an upper bound to the truncation error. We study the case $L = 2$, for which each reflection of a charge will result in a dipole, and calculate the ratio of contributions to the potential from successive reflections. Consider an nth-level image charge q_n within one sphere, at a distance r_n to the sphere center, and its image dipole produced within the other sphere at reflection level $n+1$. From (35), the potentials, at the source point, of q_n and its image charges are

$$\Phi_n = \frac{q_n}{4\pi\epsilon_0\epsilon_{\mathrm{m}}} \frac{1}{a + D/2 - r_n}, \tag{A.1}$$

$$\Phi_{n+1} = \frac{q_{n+1}}{4\pi\epsilon_0\epsilon_{\mathrm{m}}} \left(\frac{1}{a + D/2 - r_{n+1}} - \frac{1}{a + D/2 - \omega r_{n+1}} \right), \tag{A.2}$$

where $\omega = (\frac{1}{2})^{\frac{1}{\lambda}}$, $q_{n+1} = -\gamma a q_n / r_{\mathrm{s}}$, and $r_{n+1} = a^2/r_{\mathrm{s}}$, with $r_{\mathrm{s}} = r_{12} - r_n$ the source-charge location for the next-level image dipole. Defining $\nu = r_{\mathrm{s}}/a$, $\zeta = D/a$, and $\mu = 1 + \zeta/2$, we can write the absolute ratio between the two potentials $\vartheta = |\Phi_n/\Phi_{n+1}|$ as

$$\vartheta = \frac{(\mu\nu - 1)(\mu\nu - \omega)}{|\gamma|(1 - \omega)(\nu - \mu)}. \tag{A.3}$$

Thus, if we only retain terms up to level R in (35), we incur an error $\|E_T\|_\infty \sim \Phi_1/\vartheta^R$. Note that ν satisfies the inequality $2\mu^2 - 1 \le \mu\nu \le 2\mu^2$, so that

$$\vartheta \ge \frac{2\mu\sqrt{(\mu^2-1)(\mu^2-\omega)} + \mu(2\mu^2-1-\omega)}{|\gamma|(1-\omega)} . \tag{A.4}$$

Therefore the truncation error depends on μ or, equivalently, ζ, embodying the effect of the contact distance between the two spheres: Larger ζ will lead to a smaller truncation error.

The truncation error for (37) can be estimated in a similar manner, resulting in a lower bound for the potential ratio

$$\vartheta' \ge \frac{2\mu^2\sqrt{\mu^2-1} + \mu(2\mu^2-1)}{|\gamma|} . \tag{A.5}$$

Comparison of (A.4) and (A.5) shows that the estimates coincide in the conducting limit ($\epsilon_1 \gg \epsilon_m$, i.e., $\lambda \to 0$, $\omega \to 0$).

A.2. Quadrature error

We analyze the Gaussian-quadrature error $\|E_Q\|_\infty$ for the system considered in Appendix A.1. For the line charge induced by the nth image charge q_n the integrand in (34) then is

$$f(x) = \frac{\gamma a}{8\pi\epsilon_0\epsilon_m r_s\left[a + \frac{D}{2} - \frac{a^2}{r_s}\left(\frac{1-x}{2}\right)^{1/\lambda}\right]} . \tag{A.6}$$

Estimation of (34) via p-point Gauss–Legendre quadrature yields the residue

$$E_n = \frac{f^{(2p)}(\xi)q_n}{(2p)!}\int_{-1}^{1} K^2(x)dx , \tag{A.7}$$

where $K(x) = \prod_{k=0}^{p-1}(x - x_k)$ and $\xi \in [-1, 1]$. Since $|x - x_k| \le 2$, we find, denoting $\alpha_{2p} = \max_{-1\le\xi\le1}[|f^{(2p)}(\xi)|]$,

$$|E_n| \le \frac{\alpha_{2p}}{(2p)!}2^{2p+1}|q_n| . \tag{A.8}$$

The limiting cases $\lambda \to 0$ and $\lambda \to 1$ are the easiest to evaluate. Since the former corresponds to the conducting limit where the line charge reduces to a point charge, we consider $\lambda \to 1$. The $(2p)$th derivative of $f(x)$ is

$$f^{(2p)}(x) = -\frac{1}{4\pi\epsilon_0\epsilon_m a}(2p)!\left(x + \frac{2r_s}{a} + \frac{r_s D}{a^2} - 1\right)^{(-2p-1)} , \tag{A.9}$$

and then

$$\alpha_{2p} = \frac{1}{4\pi\epsilon_0\epsilon_m a}(2p)!\left(\frac{a^2/r_s}{2a + D - 2a^2/r_s}\right)^{(2p+1)} . \tag{A.10}$$

This yields an upper bound for the quadrature error in the nth-level line charge,

$$|E_n| \le \frac{|q_n|}{4\pi\epsilon_0\epsilon_m a}\left(\frac{a^2/r_s}{a + D/2 - a^2/r_s}\right)^{(2p+1)} . \tag{A.11}$$

Similarly, the quadrature error for the next-level line charges induced by the $p+1$ image charges of q_n inside the other sphere is bounded by

$$|E_{n+1}| \le \frac{|q_{n+1}|}{4\pi\epsilon_0\epsilon_m a}\left[\left(\frac{a^2/r_s'}{a + D/2 - a^2/r_s'}\right)^{(2p+1)} - \left(\frac{a^2/r_{12}}{a + D/2 - a^2/r_{12}}\right)^{(2p+1)}\right] , \tag{A.12}$$

where $r_s' = r_{12} - r_{n+1}$ is the distance of the Kelvin image charge to the other sphere, $r_{n+1} = a^2/r_s$, and r_{12} is the maximum distance of the remaining p image charges (which sum up $-q_{n+1}$) to the other sphere. Let $|E_n|_{\max}$ be the maximum quadrature error at level n. Comparing (A.11) and (A.12), we note that $|E_n|_{\max}$ varies only weakly with n for a general reflection level $n \ge 1$. On the other hand, for $n = 0$, i.e., for the initial source charge at $r_0 = a + D/2$, there is a significant difference between $|E_0|_{\max}$ and $|E_1|_{\max}$,

$$\frac{|E_0|_{\max}}{|E_1|_{\max}} \ge \left(2\mu - \frac{1}{\mu}\right)2^{2p+1} . \tag{A.13}$$

Thus, for the higher-level image reflections the number of image charges used to approximate the line charge can be reduced without much effect on the accuracy.

References

[1] Y. Levin, Electrostatic correlations: from plasma to biology, Rep. Prog. Phys. 65 (2002) 1577–1632.
[2] R.H. French, V.A. Parsegian, R. Podgornik, R.F. Rajter, A. Jagota, J. Luo, D. Asthagiri, M.K. Chaudhury, Y.-m. Chiang, S. Granick, et al., Long range interactions in nanoscale science, Rev. Mod. Phys. 82 (2010) 1887–1944.
[3] D.A. Walker, B. Kowalczyk, M. Olvera de La Cruz, B.A. Grzybowski, Electrostatics at the nanoscale, Nanoscale 3 (2011) 1316–1344.
[4] P. Debye, E. Hückel, Zur Theorie der Elektrolyte. I. Gefrierpunktserniedrigung und verwandte Erscheinungen, Phys. Z. 24 (1923) 185–206.
[5] I. Borukhov, D. Andelman, H. Orland, Steric effects in electrolytes: a modified Poisson–Boltzmann equation, Phys. Rev. Lett. 79 (1997) 435–438.
[6] J. Wang, C. Tan, Y.-H. Tan, Q. Lu, R. Luo, Poisson–Boltzmann solvents in molecular dynamics simulations, Commun. Comput. Phys. 3 (2008) 1010–1031.
[7] A.R.J. Silalahi, A.H. Boschitsch, R.C. Harris, M.O. Fenley, Comparing the predictions of the nonlinear Poisson–Boltzmann equation and the ion size-modified Poisson–Boltzmann equation for a low-dielectric charged spherical cavity in an aqueous salt solution, J. Chem. Theory Comput. 6 (2010) 3631–3639.
[8] E. Luijten, M.E. Fisher, A.Z. Panagiotopoulos, Universality class of criticality in the restricted primitive model electrolyte, Phys. Rev. Lett. 88 (2002) 185701.
[9] Y.C. Kim, E. Luijten, M.E. Fisher, Screening in ionic systems: simulations for the Lebowitz length, Phys. Rev. Lett. 95 (2005) 145701.
[10] R. Messina, Image charges in spherical geometry: application to colloidal systems, J. Chem. Phys. 117 (2002) 11062–11074.
[11] E. Bichoutskaia, A.L. Boatwright, A. Khachatourian, A.J. Stace, Electrostatic analysis of the interactions between charged particles of dielectric materials, J. Chem. Phys. 133 (2010) 024105.
[12] K. Barros, E. Luijten, Dielectric effects in the self-assembly of binary colloidal aggregates, Phys. Rev. Lett. 113 (2014) 017801.
[13] A. Diehl, A.P. dos Santos, Y. Levin, Surface tension of an electrolyte–air interface: a Monte Carlo study, J. Phys. Condens. Matter 24 (2012) 284115.
[14] D.J. Tobias, A.C. Stern, M.D. Baer, Y. Levin, C.J. Mundy, Simulation and theory of ions at atmospherically relevant aqueous liquid–air interfaces, Annu. Rev. Phys. Chem. 64 (2013) 339–359.
[15] A. van der Vaart, B.D. Bursulaya, C.L. Brooks III, K.M. Merz, Are many-body effects important in protein folding?, J. Phys. Chem. B 104 (2000) 9554–9563.
[16] G.D.J. Phillies, Excess chemical potential of dilute solutions of spherical polyelectrolytes, J. Chem. Phys. 60 (1974) 2721–2731.
[17] J.D. Love, Dielectric sphere–sphere and sphere–plane problems in electrostatics, Q. J. Mech. Appl. Math. 28 (1975) 449–471.
[18] R.B. McClurg, C.F. Zukoski, The electrostatic interaction of rigid, globular proteins with arbitrary charge distributions, J. Colloid Interface Sci. 208 (1998) 529–542.
[19] P. Linse, Electrostatics in the presence of spherical dielectric discontinuities, J. Chem. Phys. 128 (2008) 214505.
[20] R. Allen, J.-P. Hansen, Density functional approach to the effective interaction between charges within dielectric cavities, J. Phys. Condens. Matter 14 (2002) 11981–11997.
[21] I. Lotan, T. Head-Gordon, An analytical electrostatic model for salt screened interactions between multiple proteins, J. Chem. Theory Comput. 2 (2006) 541–555.
[22] A.P. dos Santos, A. Bakhshandeh, Y. Levin, Effects of the dielectric discontinuity on the counterion distribution in a colloidal suspension, J. Chem. Phys. 135 (2011) 044124.
[23] Z. Gan, Z. Xu, Multiple-image treatment of induced charges in Monte Carlo simulations of electrolytes near a spherical dielectric interface, Phys. Rev. E 84 (2011) 016705.
[24] V. Jadhao, F.J. Solis, M. Olvera de la Cruz, Simulation of charged systems in heterogeneous dielectric media via a true energy functional, Phys. Rev. Lett. 109 (2012) 223905.
[25] K. Barros, D. Sinkovits, E. Luijten, Efficient and accurate simulation of dynamic dielectric objects, J. Chem. Phys. 140 (2014) 064903.
[26] W. Thomson, Extrait d'une Lettre de M. William Thomson à M. Liouville, J. Math. Pures Appl. 10 (1845) 364–367.
[27] C. Neumann, Hydrodynamische Untersuchungen, nebst einem Anhange über die Probleme der Elektrostatik und der magnetischen Induction, B.G. Teubner, Leipzig, 1883.
[28] F. Olyslager, I.V. Lindell, Closed form solutions of Maxwell's equations in the computer age, Radio Sci. Bull. 305 (2003) 30–37.
[29] Z. Xu, W. Cai, Fast analytical methods for macroscopic electrostatic models in biomolecular simulations, SIAM Rev. 53 (2011) 683–720.
[30] Z. Xu, W. Cai, X. Cheng, Image charge method for reaction fields in a hybrid ion-channel model, Commun. Comput. Phys. 9 (2011) 1056–1070.
[31] Z. Xu, Electrostatic interaction in the presence of dielectric interfaces and polarization-induced like-charge attraction, Phys. Rev. E 87 (2013) 013307.
[32] D.G. Levitt, Electrostatic calculations for an ion channel. 1. Energy and potential profiles and interactions between ions, Biophys. J. 22 (1978) 209–219.
[33] R.J. Zauhar, R.S. Morgan, A new method for computing the macromolecular electric potential, J. Mol. Biol. 186 (1985) 815–820.
[34] H. Hoshi, M. Sakurai, Y. Inoue, R. Chûjô, Medium effects on the molecular electronic structure. I. The formulation of a theory for the estimation of a molecular electronic structure surrounded by an anisotropic medium, J. Chem. Phys. 87 (1987) 1107–1115.
[35] R. Allen, J.-P. Hansen, S. Melchionna, Electrostatic potential inside ionic solutions confined by dielectrics: a variational approach, Phys. Chem. Chem. Phys. 3 (2001) 4177–4186.
[36] D. Boda, D. Gillespie, W. Nonner, D. Henderson, B. Eisenberg, Computing induced charges in inhomogeneous dielectric media: application in a Monte Carlo simulation of complex ionic systems, Phys. Rev. E 69 (2004) 046702.
[37] P.-G. Martinsson, Fast evaluation of electro-static interactions in multi-phase dielectric media, J. Comput. Phys. 211 (2006) 289–299.
[38] S. Tyagi, M. Süzen, M. Sega, M. Barbosa, S.S. Kantorovich, C. Holm, An iterative, fast, linear-scaling method for computing induced charges on arbitrary dielectric boundaries, J. Chem. Phys. 132 (2010) 154112.
[39] R. Yokota, J.P. Bardhan, M.G. Knepley, L.A. Barba, T. Hamada, Biomolecular electrostatics using a fast multipole BEM on up to 512 GPUs and a billion unknowns, Comput. Phys. Commun. 182 (2011) 1272–1283.
[40] Y. Saad, M.H. Schultz, GMRES: a generalized minimal residual algorithm for solving nonsymmetric linear systems, SIAM J. Sci. Stat. Comput. 7 (1986) 856–869.
[41] J. Liang, S. Subramaniam, Computation of molecular electrostatics with boundary element methods, Biophys. J. 73 (1997) 1830–1841.
[42] R.W. Hockney, J.W. Eastwood, Computer Simulation Using Particles, IOP Publishing, Bristol, 1988.
[43] E.L. Pollock, J. Glosli, Comments on P^3M, FMM, and the Ewald method for large periodic Coulombic systems, Comput. Phys. Commun. 95 (1996) 93–110.
[44] J. Barnes, P. Hut, A hierarchical $O(N \log N)$ force-calculation algorithm, Nature 324 (1986) 446–449.
[45] A.W. Appel, An efficient program for many-body simulation, SIAM J. Sci. Stat. Comput. 6 (1985) 85–103.
[46] Z.-H. Duan, R. Krasny, An adaptive treecode for computing nonbonded potential energy in classical molecular systems, J. Comput. Chem. 22 (2001) 184–195.
[47] Z. Gan, Z. Xu, Efficient implementation of the Barnes–Hut octree algorithm for Monte Carlo simulations of charged systems, Sci. China Math. 57 (2014) 1331–1340.
[48] J. Wu, D. Bratko, J.M. Prausnitz, Interaction between like-charged colloidal spheres in electrolyte solutions, Proc. Natl. Acad. Sci. USA 95 (1998) 15169–15172.
[49] J.Z. Wu, D. Bratko, H.W. Blanch, J.M. Prausnitz, Monte Carlo simulation for the potential of mean force between ionic colloids in solutions of asymmetric salts, J. Chem. Phys. 111 (1999) 7084–7094.

[50] J. Liu, E. Luijten, Stabilization of colloidal suspensions by means of highly charged nanoparticles, Phys. Rev. Lett. 93 (2004) 247802.
[51] J. Liu, E. Luijten, Colloidal stabilization via nanoparticle halo formation, Phys. Rev. E 72 (2005) 061401.
[52] C.J. Martinez, J. Liu, S.K. Rhodes, E. Luijten, E.R. Weeks, J.A. Lewis, Interparticle interactions and direct imaging of colloidal phases assembled from microsphere–nanoparticle mixtures, Langmuir 21 (2005) 9978–9989.
[53] S.A. Barr, E. Luijten, Effective interactions in mixtures of silica microspheres and polystyrene nanoparticles, Langmuir 22 (2006) 7152–7155.
[54] G.I. Guerrero-García, E. González-Tovar, M. Olvera de la Cruz, Entropic effects in the electric double layer of model colloids with size-asymmetric monovalent ions, J. Chem. Phys. 135 (2011) 054701.
[55] L.D. Landau, E.M. Lifshitz, L.P. Pitaevskii, Electrodynamics of Continuous Media, 2nd edition, Course of Theoretical Physics, vol. 8, Elsevier Butterworth Heinemann, Oxford, 1993.
[56] L. Greengard, V. Rokhlin, A fast algorithm for particle simulations, J. Comput. Phys. 73 (1987) 325–348.
[57] L. Greengard, V. Rokhlin, A new version of the Fast Multipole Method for the Laplace equation in three dimensions, Acta Numer. 6 (1997) 229–269.
[58] H. Cheng, L. Greengard, V. Rokhlin, A fast adaptive multipole algorithm in three dimensions, J. Comput. Phys. 155 (1999) 468–498.
[59] L. Ying, G. Biros, D. Zorin, A kernel-independent adaptive fast multipole algorithm in two and three dimensions, J. Comput. Phys. 196 (2004) 591–626.
[60] M. Hoyles, S. Kuyucak, S.-H. Chung, Solutions of Poisson's equation in channel-like geometries, Comput. Phys. Commun. 115 (1998) 45–68.
[61] J.-L. Guermond, Numerical quadratures for layer potentials over curved domains in $\mathbb{R}^3$, SIAM J. Numer. Anal. 29 (1992) 1347–1369.
[62] J.P. Bardhan, M.D. Altman, D.J. Willis, S.M. Lippow, B. Tidor, J.K. White, Numerical integration techniques for curved-element discretizations of molecule-solvent interfaces, J. Chem. Phys. 127 (2007) 014701.
[63] C. Berti, D. Gillespie, J.P. Bardhan, R.S. Eisenberg, C. Fiegna, Comparison of three-dimensional Poisson solution methods for particle-based simulation and inhomogeneous dielectrics, Phys. Rev. E 86 (2012) 011912.
[64] J.G. Kirkwood, Theory of solutions of molecules containing widely separated charges with special application to zwitterions, J. Chem. Phys. 2 (1934) 351–361.
[65] J.D. Jackson, Classical Electrodynamics, 3rd edition, Wiley, New York, 1999.
[66] W. Cai, S. Deng, D. Jacobs, Extending the fast multipole method to charges inside or outside a dielectric sphere, J. Comput. Phys. 223 (2007) 846–864.
[67] Z. Xu, A fast algorithm for treating dielectric discontinuities in charged spherical colloids, Interdiscip. Sci. Comput. Life Sci. 4 (2012) 19–26.
[68] H.A. Boateng, R. Krasny, Comparison of treecodes for computing electrostatic potentials in charged particle systems with disjoint targets and sources, J. Comput. Chem. 34 (2013) 2159–2167.
[69] K. Binder, E. Luijten, Monte Carlo tests of renormalization-group predictions for critical phenomena in Ising models, Phys. Rep. 344 (2001) 179–253.
[70] P. Linse, Simulation of charged colloids in solution, Adv. Polym. Sci. 185 (2005) 111–162.
[71] D. Gillespie, M. Valiskó, D. Boda, Density functional theory of the electrical double layer: the RFD functional, J. Phys. Condens. Matter 17 (2005) 6609–6626.
[72] S. Asakura, F. Oosawa, On interaction between two bodies immersed in a solution of macromolecules, J. Chem. Phys. 22 (1954) 1255–1256.
[73] S. Asakura, F. Oosawa, Interaction between particles suspended in solutions of macromolecules, J. Polym. Sci. 33 (1958) 183–192.